

ARTICLE

Received 12 Dec 2013 | Accepted 22 Apr 2014 | Published 29 May 2014

DOI: 10.1038/ncomms4927

Kondo physics in non-local metallic spin transport devices

L. O'Brien^{1,2}, M.J. Erickson³, D. Spivak³, H. Ambaye⁴, R.J. Goyette⁴, V. Lauter⁴, P.A. Crowell³ & C. Leighton¹

The non-local spin-valve is pivotal in spintronics, enabling separation of charge and spin currents, disruptive potential applications and the study of pressing problems in the physics of spin injection and relaxation. Primary among these problems is the perplexing non-monotonicity in the temperature-dependent spin accumulation in non-local ferromagnetic/non-magnetic metal structures, where the spin signal decreases at low temperatures. Here we show that this effect is strongly correlated with the ability of the ferromagnetic to form dilute local magnetic moments in the NM. This we achieve by studying a significantly expanded range of ferromagnetic/non-magnetic combinations. We argue that local moments, formed by ferromagnetic/non-magnetic interdiffusion, suppress the injected spin polarization and diffusion length via a manifestation of the Kondo effect, thus explaining all observations. We further show that this suppression can be completely quenched, even at interfaces that are highly susceptible to the effect, by insertion of a thin non-moment-supporting interlayer.

¹Department of Chemical Engineering and Materials Science, University of Minnesota, Minneapolis, Minnesota 55455, USA. ²Thin Film Magnetism, Department of Physics, Cavendish Laboratory, University of Cambridge, Cambridge CB3 0HE, UK. ³School of Physics and Astronomy, University of Minnesota, Minneapolis, Minnesota 55455, USA. ⁴Neutron Sciences Directorate, Oak Ridge National Laboratory, Oak Ridge, Tennessee 37831, USA. Correspondence and requests for materials should be addressed to C.L. (email: leighton@umn.edu)

Spintronic devices based on metals and insulators have been remarkably successful, as illustrated by the universal use of spin-valves, and now magnetic tunnel junctions, in hard disk read sensors. The need to scale such devices to extremely small sizes introduces serious impedance matching and noise issues, however, making all-metallic structures (for example, current-perpendicular-to-plane giant magnetoresistance stacks)¹ attractive for next-generation devices². Remarkably, despite the maturity of metallic spintronics, there remain large gaps in our fundamental understanding of spin transport in metals, particularly with injection of spins across ferromagnet (FM)/non-magnetic metal (NM) interfaces, and their subsequent diffusion and relaxation. Unresolved issues include the applicability of the widely employed Elliott-Yafet (E-Y)³ spin relaxation mechanism^{4–10}, the influence of defects, surfaces and interfaces on spin relaxation at nanoscopic dimensions^{8,11–15}, the importance of magnetic and spin-orbit scattering^{16–18} and the accuracy of existing models^{19–23}.

In the quest to understand such issues, the non-local spin valve (NLSV)²⁴ has a pivotal role as it enables separation of charge and spin currents, providing a direct means to study spin injection, transport and relaxation²⁵. In the NLSV geometry, two nanoscopic FM electrodes separated a distance d are electrically connected via a nanoscopic NM (that is, para- or dia-magnetic) channel. A spin-polarized charge current I_Q is injected from one FM (FM_{inj}), and extracted from the far edge of the NM, away from the second FM electrode (FM_{det}). Ideally, in this geometry, no charge current flows between the two FM contacts. A non-equilibrium spin polarization thus accumulates above FM_{inj} and diffuses, in both directions, along the NM channel, generating a

diffusive pure spin current (I_s) between FM_{inj} and FM_{det} . Some fraction of the injected spins reach FM_{det} , generating a non-local spin-dependent potential difference, V_{NL} (and a non-local resistance, $R_{NL} = V_{NL}/I_Q$) between FM_{det} and the right edge of the NM. The magnetizations of FM_{inj} and FM_{det} are then switched between parallel (P) and antiparallel (AP) to determine $\Delta R_{NL} = R_P - R_{AP}$, a direct measure of the spin accumulation at FM_{det} , devoid of complications due to charge currents. $\Delta R_{NL}(d)$ can then be used to determine, via an appropriate model^{19,21,22,25}, parameters such as the spin polarization of the injected current (α) and the NM spin diffusion length (λ_N).

This non-local geometry has enabled significant advances in the understanding of spin transport in metals^{4–16,18,22,24–37}, but has also highlighted serious discrepancies with theory. The primary example of the latter is the surprising non-monotonicity in the temperature (T) dependence of ΔR_{NL} , and thus the deduced λ_N , in the transparent interface limit. In the widely investigated $Ni_{80}Fe_{20}/Cu$, for example, ΔR_{NL} initially increases on cooling but then drops (by 10–40%, dependent on dimensions) below ~ 40 K (refs 8,10,18,30–33). This is in stark contrast to expectations from the E-Y mechanism^{17,38}, which posits $\tau_s \propto \tau_p$ (where τ_s is the NM spin lifetime and τ_p the momentum relaxation time), that is, that spin relaxation occurs with finite probability at each momentum scattering event ($\sim 1 \times 10^{-3}$ for pure Cu³⁸). A monotonic decrease in NM resistivity (ρ_N) on cooling implies a monotonic increase in τ_p , and thus a monotonic increase in τ_s and λ_N , in direct contradiction with observations. This anomalous behaviour has proven very difficult to explain. Surface spin relaxation¹⁰, reduced dimensions⁹ and surface¹⁸/bulk⁸ (magnetic) impurities have all been advanced, but no

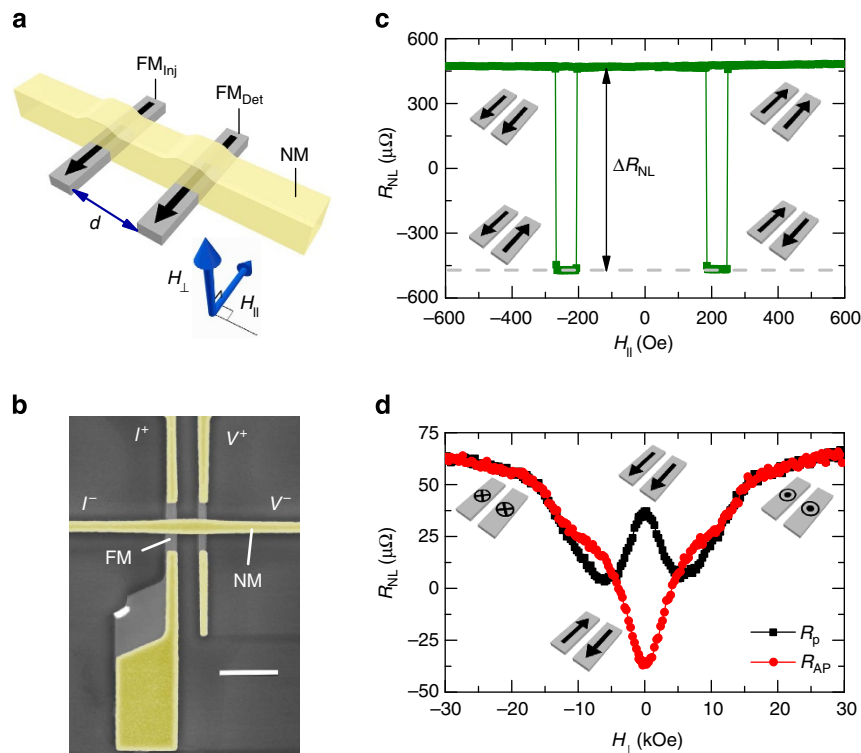


Figure 1 | Non-local spin valve experimental geometry and field-dependence of the non-local resistance R_{NL} . (a) Schematic of the experimental NLSV geometry showing ferromagnet (FM) and non-magnetic metal (NM) materials, the inter-FM separation (d) and the field orientation for parallel, $H_{||}$, and perpendicular, H_{\perp} , alignment. (b) False colour scanning electron microscope image of a $d = 250$ nm Fe/Cu device showing current (I) and voltage (V) contact orientations (with a 500 nm scale bar). (c) In-plane field dependence of R_{NL} for a $Ni_{80}Fe_{20}/Al$ device with $d = 250$ nm at temperature, $T = 50$ K, with $\Delta R_{NL} = R_P - R_{AP}$ indicated. (d) Out-of-plane (Hanle geometry) field dependence of the parallel, R_P (black squares), and anti-parallel, R_{AP} (red circles), non-local resistance for an Fe/Cu device with $d = 2 \mu m$ at $T = 50$ K. The schematic labels shown in (c,d) indicate the orientation of FM injector and detector.

consensus has emerged. One issue contributing to this is the focus on only a small set of materials, with $\text{Ni}_{80}\text{Fe}_{20}/\text{Cu}$ and $\text{Ni}_{80}\text{Fe}_{20}/\text{Ag}$ accounting for a major fraction of prior work^{10,18,28,30–35,39}.

In this work, via systematic studies significantly expanding the range of FM and NM materials investigated (encompassing $\text{Ni}_{80}\text{Fe}_{20}$, Ni, Fe, Co, Cu and Al), we show that in devices where the FM and NM are synthesized in a single deposition sequence, the low T downturn in ΔR_{NL} is not a property of an individual NM but rather of the FM/NM pair. NM materials that do not support local magnetic moments when a given FM is diluted in them are found to show no low T anomalies, exemplified by Al. For the FM/NM pairs that do exhibit the anomalous non-monotonicity, we provide strong evidence that FM/NM interdiffusion leads to the formation of local moments which suppress α , and to a lesser extent λ_{N} , via a manifestation of the Kondo effect. We further show that this suppression can be quenched by ultra-thin non-moment-supporting interlayers (ILs). We argue that these concepts provide a coherent explanation of all major features of the available data, with implications even for room temperature spin transport.

Results

Field dependence of the non-local resistance. A schematic of the NLSV geometry employed in our work is shown in Fig. 1a; a typical ($d=250$ nm) NLSV device is shown in the scanning electron microscope image of Fig. 1b. The FM electrodes have widths $w_{\text{FM,inj}}$ and $w_{\text{FM,det}}$, and thickness t_{FM} , whereas the NM channel has width w_{N} and thickness t_{N} . Unless otherwise noted, devices in this work have $t_{\text{FM}}=16$ nm and $t_{\text{N}}=200$ nm. In Fig. 1c,d, we first illustrate the basic response of R_{NL} to in-plane and perpendicular-to-plane magnetic fields (H_{\parallel} and H_{\perp} , Fig. 1a). Figure 1c shows $R_{\text{NL}}(H_{\parallel})$ for a $d=250$ nm $\text{Ni}_{80}\text{Fe}_{20}/\text{Al}$ device at $T=50$ K, the labels showing the magnetization orientation of FM_{inj} and FM_{det} . As is typical²⁶, a small field-independent background ($16\ \mu\Omega$ here) has been subtracted. Complete and abrupt switching between P and AP is observed, enabling determination of ΔR_{NL} , the T and d dependence of which allow for extraction of $\alpha(T)$ and $\lambda_{\text{N}}(T)$. Figure 1d shows the dependence of R_{P} and R_{AP} on H_{\perp} , for a $d=2\ \mu\text{m}$ Fe/Cu device at $T=50$ K. The gradually damped oscillations derive from the Hanle effect^{12,23,25,29,36,37,39} (because of the precession of the diffusing spins about H_{\perp}), R_{P} and R_{AP} merging at high H_{\perp} when FM_{inj} and FM_{det} are driven out of plane (see schematics, Fig. 1d). Such data enable extraction of τ_{s} , and thus $\lambda_{\text{N}} = \sqrt{\tau_{\text{s}}D}$ (where D is the electron diffusivity), complementary to that from $\Delta R_{\text{NL}}(d)$.

Varying FM/NM material combinations. Before detailed analysis of $\alpha(T)$, $\lambda_{\text{N}}(T)$ and $\tau_{\text{s}}(T)$, we first present a central observation of this work, arrived at by studying $\Delta R_{\text{NL}}(T)$ in a large set of materials (Fig. 2). The data are from NLSVs with $d=250$ nm, and a logarithmic T axis is chosen to illustrate the low T behaviour. Figure 2a focuses on Cu channels with Fe, $\text{Ni}_{80}\text{Fe}_{20}$, Co and Ni, Fig. 2b on Cu channels with $\text{Ni}_{100-x}\text{Fe}_x$ ($x=0, 20$ and 100), and Fig. 2c on Al with Fe, $\text{Ni}_{80}\text{Fe}_{20}$ and Co. Beginning with Fig. 2a, we first note the $\Delta R_{\text{NL}}(T)$ for $\text{Ni}_{80}\text{Fe}_{20}/\text{Cu}$, which indeed shows the anomalous decrease below ~ 40 K (refs 8,10,18,30–33). Considering Co, Fe and Ni, however, it can be seen that the low T downturn in $\Delta R_{\text{NL}}(T)$ is obviously not a property of the NM alone, but is strongly influenced by the FM. Specifically, Fe/Cu shows the strongest downturn (onset temperature of 60 K), followed by $\text{Ni}_{80}\text{Fe}_{20}/\text{Cu}$ (40 K onset), and then Co/Cu, where the effect is weak but occurs below ~ 130 K. In Ni/Cu on the other hand, we find no evidence for a low T downturn in $\Delta R_{\text{NL}}(T)$. The $\text{Ni}_{100-x}\text{Fe}_x/\text{Cu}$ case is particularly interesting and is highlighted in Fig. 2b, where data

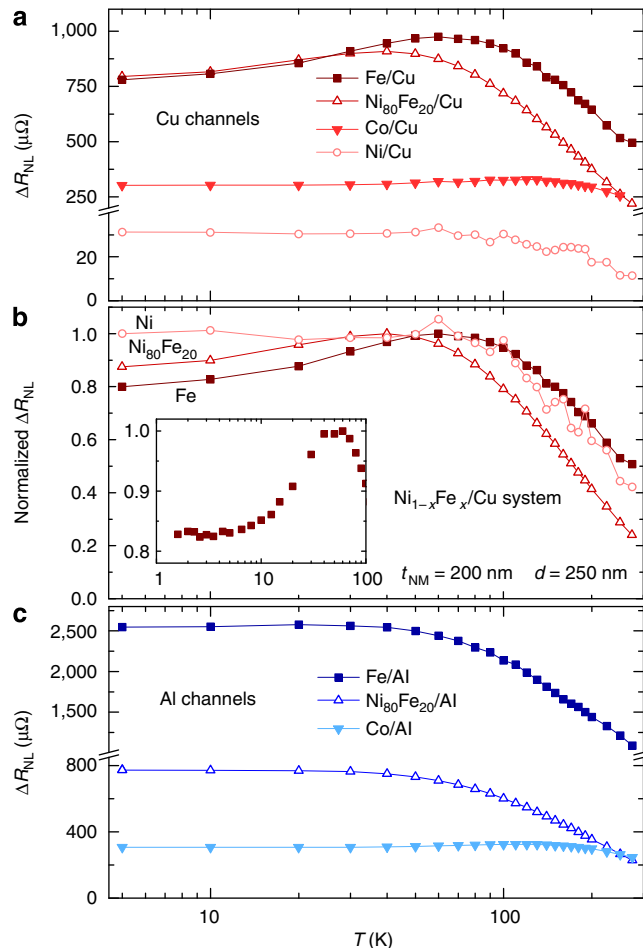


Figure 2 | Temperature dependence of the spin accumulation signal for various ferromagnet/non-magnetic metal material pairings. (a) Spin accumulation signal, ΔR_{NL} , as a function of temperature, T , (log scale) for various ferromagnet FM materials, using Cu (red data) as the non-magnetic metal NM channel material. The FM contact material is indicated by: Fe, closed squares; $\text{Ni}_{80}\text{Fe}_{20}$, open triangles; Co, closed triangles; Ni, open circles. (b) Normalized ΔR_{NL} as a function of T for the $\text{Ni}_{1-x}\text{Fe}_x/\text{Cu}$ system. The inset shows a plot of the normalized ΔR_{NL} versus T at low temperatures for Fe/Cu, highlighting the saturation as $T \rightarrow 0$. (c) ΔR_{NL} , as a function of T (log scale) for various FM materials, using Al (blue data) as the NM channel material. All displayed data are obtained from $d=250$ nm devices, with NM thickness, $t_{\text{NM}}=200$ nm.

for Ni, $\text{Ni}_{80}\text{Fe}_{20}$ and Fe are shown normalized to the maximum ΔR_{NL} . A clear progression is apparent. One interpretation, which we return to below, is that the low T downturn in $\Delta R_{\text{NL}}(T)$ only occurs in $\text{Ni}_{80}\text{Fe}_{20}/\text{Cu}$ because of the presence of Fe. Additional important information is obtained by extending the T range down to ~ 1 K. As shown in the inset to Fig. 2b (for Fe/Cu), the suppression of ΔR_{NL} in fact saturates at low T , below ~ 5 K in this case. Finally, turning to Fig. 2c, we find radically different behaviour with Al channels. In Al devices, no significant low T suppression is observed for any FM, $\Delta R_{\text{NL}}(T)$ monotonically increasing on cooling, qualitatively consistent with the E-Y mechanism. A number of other trends are also apparent in Fig. 2, such as the influence of the FM on the high T behaviour. The T dependence in this region strengthens as the FM is varied from $\text{Ni}_{80}\text{Fe}_{20} \rightarrow \text{Ni} \rightarrow \text{Fe} \rightarrow \text{Co}$, which we ascribe to the influence of Curie temperature (T_{C}) and magneto-crystalline anisotropy on $\alpha(T)$. FMs such as Co, with high T_{C} and relatively large anisotropy, are expected to present weak $\alpha(T)$, whereas FMs such as

$\text{Ni}_{80}\text{Fe}_{20}$ and Ni, with lower T_C and anisotropy, should have stronger $\alpha(T)$ ⁴⁰. A second observation is the large variation in $\Delta R_{\text{NL}}(T=0)$, which spans 30–2,500 $\mu\Omega$. Although a number of factors contribute, particularly the resistivities of the FM and NM (ρ_{FM} and ρ_{N}), $\alpha(T=0)$ is a dominant parameter. It accounts in particular for the low ΔR_{NL} in Ni, where α is significantly smaller than in Co, $\text{Ni}_{80}\text{Fe}_{20}$ and Fe (refs 41,42).

Fitting $\Delta R_{\text{NL}}(d)$ and the Hanle effect. To further investigate such issues, particularly the low T decrease in ΔR_{NL} , $\alpha(T)$ and $\lambda_{\text{N}}(T)$ were extracted from $\Delta R_{\text{NL}}(d, T)$, focusing on Fe/Cu (with the strongest downturn) and Fe/Al (no downturn). Such data are shown in Fig. 3a,b, where $\Delta R_{\text{NL}}(d)$ is plotted at various T . The solid lines are fits using an analytical solution^{20,21} to the NLSV spin diffusion problem in 1-D:

$$\Delta R_{\text{NL}} = 4 \frac{\alpha^2 R_{\text{FM}}^2}{(1 - \alpha^2)^2 R_{\text{N}}} \frac{\exp\left(-\frac{d}{\lambda_{\text{N}}}\right)}{\left[1 + \frac{2R_{\text{FM}}}{(1 - \alpha^2)R_{\text{N}}}\right]^2 - \exp\left(-\frac{2d}{\lambda_{\text{N}}}\right)}, \quad (1)$$

where $\alpha = I_{\uparrow} - I_{\downarrow} / I_{\uparrow} + I_{\downarrow}$ is the current polarization of the FM, λ_{FM} is the spin diffusion length in the FM, and $R_{\text{N}} = \rho_{\text{N}} \lambda_{\text{N}} / w_{\text{N}} t_{\text{N}}$ and $R_{\text{FM}} = \rho_{\text{FM}} \lambda_{\text{FM}} / w_{\text{FM}} t_{\text{N}}$ are the N and FM spin resistances. This expression applies in the transparent interface limit, that is, interface resistance $< R_{\text{N}}, R_{\text{FM}}$, which we verify to be the case here (see Supplementary Figs 1 and 2 and Supplementary Notes 1 and 2). All geometrical parameters in equation (1) were measured for each device, as were $\rho_{\text{N}}(T)$ and $\rho_{\text{FM}}(T)$ (see Supplementary Fig. 2 and Supplementary Note 2). This nevertheless leaves $\alpha(T)$, $\lambda_{\text{FM}}(T)$ and $\lambda_{\text{N}}(T)$ as free parameters, resulting in poorly constrained fitting. Specifically, although $\lambda_{\text{N}}(T)$ determines the d dependence of ΔR_{NL} , and can be independently extracted (particularly in the $d > \lambda_{\text{N}}$ limit where an exponential fall-off is recovered), $\alpha(T)$ and $\lambda_{\text{FM}}(T)$ control the magnitude of ΔR_{NL} and are inseparable, entering through $\lambda_{\text{FM}} / (1 - \alpha^2)$. Constraints on one of λ_{FM} or α are thus required. As a starting point, we simply hold λ_{Fe} constant at 4 nm, a value determined from the measured $\rho_{\text{Fe}}(T=5\text{K})$ via the observed scaling between λ_{FM} and ρ_{FM} ⁴³. The resulting $\lambda_{\text{N}}(T)$ is shown in Fig. 3g,h, labelled as ‘Cu, NLSV’ and ‘Al, NLSV’, while $\alpha(T)$ is shown in Fig. 3i,j. In the Fe/Al case, both α and λ_{N} increase monotonically on cooling. However, Fe/Cu is more complex. As shown in Fig. 3g, $\lambda_{\text{N}}(T)$ increases down to 50 K, below which it appears to undergo a slight decrease. This decrease is barely above experimental uncertainty, however, amounting to $6 \pm 6\%$ based on our best error estimates. In contrast, a clear and statistically significant decrease in α is found as T is lowered below 50 K (Fig. 3i). As ΔR_{NL} at $d = 250$ nm is more sensitive to α than λ_{N} (from equation (1), see Supplementary Fig. 3 and Supplementary Note 3), this 15% decrease in α corresponds to a 28% decrease in ΔR_{NL} , the majority of the observed suppression. We thus conclude that the low T downturn in ΔR_{NL} in our NLSVs, although containing some contribution from enhanced spin relaxation, is dominated by d -independent suppression of the spin injection/detection efficiency. Exhaustive fitting, with a multitude of parameter constraints (see Supplementary Fig. 3 and Supplementary Note 3), confirms this.

As discussed above, $R_{\text{NL}}(H_{\perp})$, via the Hanle effect, provides access to τ_s , and an independent check of $\lambda_{\text{N}}(T)$. In Fig. 3c,d, we thus plot $\Delta R_{\text{NL}}(H_{\perp}) = [R_{\text{P}}(H_{\perp}) - R_{\text{AP}}(H_{\perp})] / [R_{\text{P}}(0) - R_{\text{AP}}(0)]$, at various T , for Fe/Cu and Fe/Al at $d = 2 \mu\text{m}$. (This was recorded for positive and negative H_{\perp} , but we plot here only the symmetric component.) Such large d is used to enable fitting with analytical expressions for spin diffusion-precession (see Methods), with no need to account for back-diffusion of injected spins²³. The width and amplitude of the oscillations in Fig. 3c,d are controlled solely by τ_s and D , and the fits (solid lines) use $D(T)$ determined from

the measured $\rho_{\text{N}}(T)$, resulting in the $\tau_s(T)$ shown in Fig. 3e,f. For both Fe/Cu and Fe/Al, τ_s is remarkably flat above 70 K, a dramatic illustration of the dominance of defects (for example, non-magnetic point-defects, grain boundaries) in spin relaxation. In accord with the E-Y mechanism, T -independent momentum relaxation processes associated with such defects result in T -independent spin relaxation. For Fe/Cu only (Fig. 3e), the situation is markedly different below 70 K, where τ_s drops from 12 to 7 ps, clearly correlated with $\Delta R_{\text{NL}}(T)$. Despite this substantial decrease in τ_s , the corresponding drop in $\lambda_{\text{N}} = \sqrt{\tau_s D}$ (Fig. 3g, ‘Cu, Hanle’) is small due to the increase in D (from $1/\rho_{\text{N}}$) on cooling. The overall agreement between λ_{N} determined from $\Delta R_{\text{NL}}(d)$ and from the Hanle effect is excellent (Fig. 3g,h), and the form of $\lambda_{\text{N}}(T)$ for Fe/Cu is confirmed.

The observation that the downturn in $\Delta R_{\text{NL}}(T)$ in our devices is dominated by $\alpha(T)$ (with only a secondary contribution from $\lambda_{\text{N}}(T)$), and is highly sensitive to the FM/NM pairing, is inconsistent with ‘channel only’ explanations, such as surface spin relaxation. This is underscored by the additional observation (for example, in $\text{Ni}_{80}\text{Fe}_{20}/\text{Cu}$, Supplementary Fig. 4 and Supplementary Note 4) that the ΔR_{NL} suppression is t_{N} independent⁸. Rather, the dominance of $\alpha(T)$ and sensitivity to FM/NM pairing point to explanations based on low T suppression of spin injection/detection efficiency at the interfaces. One general possibility for such is the formation of non-trivial interfacial magnetic states at low T because of FM/NM interdiffusion, such as spin-glass-like interfaces (potentially depolarizing the injected spin current), or non-collinear states (preventing full polarization). To investigate such possibilities, we undertook detailed T -dependent polarized neutron and X-ray reflectivity measurements on $\text{Ni}_{80}\text{Fe}_{20}/\text{Cu}$ and Co/Cu bilayers deposited under identical conditions to our NLSVs. The data (Supplementary Figs 5 and 6 and Supplementary Notes 5 and 6) reveal remarkably T -independent magnetic depth profiles, however, ruling out even minor changes in the interfacial magnetic structure at low T . In $\text{Ni}_{80}\text{Fe}_{20}/\text{Cu}$, for example, the magnetic interface width is only 0.6 nm, with no apparent T dependence.

Local moments and the Kondo effect in spin transport. This confinement of strong FM/NM intermixing to a thin region close to the interface does not, however, rule out explanations based on low densities of FM impurities in the NM, whether from interdiffusion, residual FM vapour pressure during NM deposition, contamination of the NM source material⁸ or other sources¹⁸. Table 1, which compares the ability of Cu and Al to host local magnetic moments when the FMs used in this work are added as dilute impurities, reveals some striking correlations in this context. $3d$ elements form local moments only when diluted in certain NMs^{44–46}, a fact that can be understood within the Anderson virtual bound state model^{44,45}, where the local moment is dictated by the relative magnitudes of the NM Fermi energy (E_{F}), s - d hybridization potential and FM intra-atomic d - d Coulomb repulsion. In Al, for example, the high E_{F} locates both up-spin and down-spin virtual bound states below the Fermi surface, quenching local moments^{44–46}. Considering Table 1, the correlation between local moment formation and the occurrence of a low T downturn in $\Delta R_{\text{NL}}(T)$ in a given FM/NM pair is in fact striking, the only apparent anomaly being Ni/Cu, as discussed below.

Importantly, in the cases where local moments do form, the Kondo effect^{44–49} is anticipated. Essentially, delocalized electrons in the NM are expected to screen the local moments from dilute FM impurities around some characteristic T scale, T_{K} (refs 45,46). Table 1 shows not only that the downturn in $\Delta R_{\text{NL}}(T)$ correlates

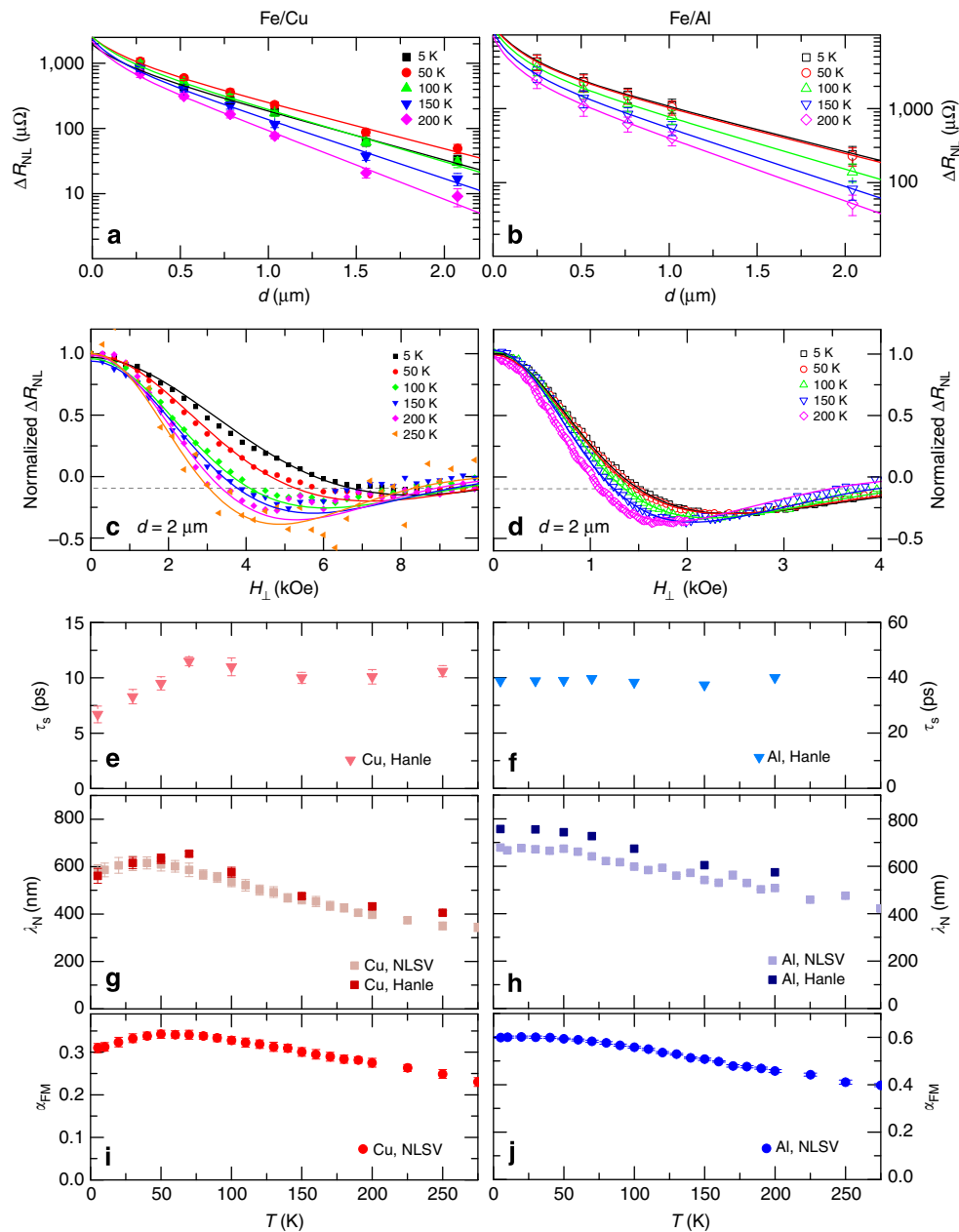


Figure 3 | Comparison between fitted parameters from Hanle and non-local spin valve (NLSV) geometries for Fe/Cu (left column, closed symbols) and Fe/Al (right column, open symbols) devices. (a,b) Ferromagnet (FM) separation (d) dependence of spin accumulation signal, ΔR_{NL} , for various temperatures, T . Solid lines are fits using the 1-D Valet-Fert model described in the text, constraining the ferromagnet spin diffusion length, λ_{FM} , to 4 nm. Error bars are the estimated total uncertainty obtained by combining in quadrature the standard error in the spin accumulation signal with systematic uncertainties in the device geometry. **(c,d)** Perpendicular magnetic field, H_{\perp} , dependence of ΔR_{NL} (Hanle geometry), normalized to $\Delta R_{\text{NL}}(H_{\perp} = 0)$, for various T . Solid lines are fits using a 1-D spin diffusion model including: effects of finite contact width, rotation of FMs and diffusivity, $D(T)$, determined from the non-magnetic metal (NM) resistivity, $\rho_{\text{N}}(T)$. The grey dashed line indicates $\Delta R_{\text{NL}} = 0$. **(e,f)** NM spin lifetime, τ_{s} , obtained from fitting Hanle effect data **(c,d)**. **(g,h)** Comparison of NM spin diffusion length, $\lambda_{\text{N}}(T)$, obtained from fitting the NLSV separation dependence (lighter colors; $\lambda_{\text{FM}} = 4$ nm) and Hanle effect measurements (darker colours; $D(T)$ constrained by $\rho_{\text{N}}(T)$). **(i,j)** Current polarization, α , obtained from fitting NLSV separation dependence.

with the formation of local moments, but moreover, that the observed downturn temperature (T_{max}) correlates with T_{K} . For Ni in Cu, for example, although dilute moments form, the extremely high T_{K} ($> 1,000$ K) precludes observation of Kondo physics at $T \leq 300$ K, consistent with observations. For Fe in Cu on the other hand, $T_{\text{K}} = 30$ K (ref. 44), comparing reasonably to $T_{\text{max}} = 60$ K for Fe/Cu and $T_{\text{max}} = 40$ K for $\text{Ni}_{80}\text{Fe}_{20}/\text{Cu}$. Note that in the latter case, because of the prohibitively high T_{K} for Ni in Cu, only Fe impurities contribute to the changes of $\Delta R_{\text{NL}}(T)$ over the measured T range, consistent with the larger downturn in Fe than

$\text{Ni}_{80}\text{Fe}_{20}$ (Fig. 2b). For Co in Cu, we observe only a weak downturn, with $T_{\text{max}} = 130$ K. The limited solubility in this case limits the strength of Kondo effects, whereas the 130 K T_{max} is consistent with the $23 \text{ K} < T_{\text{K}} < 500 \text{ K}$ bound from known limits for surface and bulk Co impurities in Cu (refs 44,47). This Kondo-suppressed spin accumulation picture is also consistent with literature observations in the heavily studied $\text{Ni}_{80}\text{Fe}_{20}/\text{Ag}$ system^{5,29,35,36}, including the existence of a downturn (because of local Fe moments in Ag), the relatively weak decrease in ΔR_{NL} (7%, because of low miscibility) and the approximate

Table 1 | Comparison between the Kondo temperature T_K and the T at which a maximum in $\Delta R_{NL}(T)$ occurs, T_{max} .

	Cu		Al	
	T_K (K)	T_{max} (K)	T_K (K)	T_{max} (K)
Ni	>1,000	Not observed	No local moments	—
Ni ₈₀ Fe ₂₀	30	40	No local moments	Not observed
Fe	30	60	No local moments	Not observed
Co	23/500*	130	No local moments	120†

For T_{max} , 'not observed' indicates no significant downturn is observable in our experimental temperature range. 'No local moments' indicates the ferromagnet (FM) impurity atom is known to not form a local moment in the given non-magnetic metal (NM) host. As Ni has a very high value of T_K , no consequences of the Kondo effect are expected to be observable in the investigated temperature range for this FM. The table is colour coded for ease of interpretation: Green—Kondo effect expected and indeed observed; red—Kondo effect not expected and indeed not observed. T_K values are taken from refs 44,47,49 and are theoretically described by $T_K = \frac{D}{k_B} \exp[-1/[N(E_F)J]]$, where D is the host conduction (s electron) bandwidth, and $N(E_F)$ is the density of states at the Fermi level. The dependence on the transition metal impurity enters through the s - d exchange coupling, $J = 2|V_{sd}|^2 U/[E_d(E_d + U)]$, where V_{sd} denotes the s - d hybridization potential, U the d - d Coulomb splitting and E_d the position of the impurity d -level relative to E_F . In Cu, an increase in J as the impurity metal varies from Fe→Co→Ni causes T_K to dramatically increase from $O(10\text{K})$ to $O(1,000\text{K})$, as shown in the table.

*Two values of T_K for Co/Cu are quoted, corresponding to the introduction of Co impurities at the surface and bulk of Cu, respectively. This complication arises due to low solubility. Note that the temperature at which a small downturn is observed in our Co/Cu data (that is, 130 K) is between the surface and bulk T_K .

†A slight downturn is observable in our experimental data for Co/Al but is likely due to phenomena other than the Kondo effect, as discussed in Supplementary Note 2 and Supplementary Fig. 2.

correspondence between T_{max} ($< 20\text{K}$) and T_K ($\sim 5\text{K}$ for Fe/Ag). Taken as a whole, the correlations between moment formation, T_K , and the magnitude and onset temperature of the downturn in ΔR_{NL} are thus remarkably strong across a wide variety of materials, revealing a simple pattern to the apparently complexity in Fig. 2.

Given these strong correlations with moment formation, miscibility and T_K , we propose a scenario where dilute quantities of FM impurities in the near-interface region of the NM lead to a novel manifestation of the Kondo effect. We suggest that the disordered local moments (and the accompanying conduction electron screening) depolarize the injected spin current at temperatures around T_K , reducing the polarization injected into the bulk of the channel (see Supplementary Fig. 7 and Supplementary Note 7). Although such physics has not been previously discussed in NLSVs, the reciprocal role of spin injection on the Kondo effect in charge transport has been explored⁴⁸, and some precedent for related effects exists in magnetic tunnel junctions⁵⁰. Critically, we believe that this picture provides qualitative explanations for all observed phenomena. The absence of a downturn in Al-based devices, the miscibility-related magnitude in FM/Cu and the correlation between T_{max} and T_K are all straightforwardly understood. Regarding the latter it should be noted that in this picture T_{max} will be determined by the competition between the Kondo suppression of the spin accumulation and the usual $\alpha(T)$, $\lambda(T)$ and $\rho(T)$, meaning that the correlation between T_K and T_{max} is expected to be only approximate, as is the case. Our model also explains the saturation of the downturn in $\Delta R_{NL}(T)$ at very low T in Fe/Cu (Fig. 2b, inset), as the Kondo suppression of α should saturate at $T \ll T_K$, because of inter-moment d - d interactions and entry into the unitary scattering limit^{44–46}. Note that the fact that we observe no conventional Kondo effect in direct four-terminal $\rho_N(T)$ measurements on our devices (see Supplementary Figs 2 and 4 and Supplementary Notes 2 and 4) in no way contradicts this picture. The charge current in such measurements will be dominated by the highest conductivity central regions of the NM channel, the near-interface regions relatively rich in FM impurities having little influence on $\rho_N(T)$. This would be expected to change if interdiffusion were promoted to the extent that the bulk of the NM channel reached FM concentrations $> O(1\text{p.p.m.})$, where the Kondo effect emerges. To demonstrate this directly, we thermally annealed a $d = 250\text{nm}$ Fe/Cu device for 2 h under high vacuum at 500°C , resulting in the $\rho_N(T)$ shown in the inset of Fig. 4a, where a clear Kondo minimum occurs. The $\rho_N(T)$ curve can in fact be fit to an empirical relation⁵¹ for the Kondo effect (purple solid line, see Methods) with $T_K = 30\text{K}$, yielding a Kondo resistivity,

$\rho_K = 0.06\ \mu\Omega\text{cm}$, and a resistivity minimum at 20.5K . The latter is consistent with an average Fe concentration of $100\text{--}200\text{p.p.m.}$ (ref. 52). Most importantly, examining $\Delta R_{NL}(T)$ for such a device (Fig. 4a), we find a substantial enhancement of the downturn, ΔR_{NL} being reduced by $\sim 50\%$ below a T_{max} that now exceeds 100K . These results prove that Kondo physics is active in charge transport in our devices and that the anomaly in $\Delta R_{NL}(T)$ is indeed enhanced as the charge Kondo effect is promoted, as expected.

A final point to emphasize regarding the Kondo suppression of $\Delta R_{NL}(T)$ is that while in our case the role of $\alpha(T)$ is dominant over $\lambda_N(T)$, this balance could vary with synthesis conditions. Deposition of the FM and NM in separate systems¹⁰, contamination of the NM source with FM impurities⁵³ and transfer of FM impurities to the NM channel from resists¹⁸ will change the balance between FM/NM interface and bulk channel magnetic impurity contributions, altering the relative contributions of $\alpha(T)$ and $\lambda_N(T)$ to the downturn in ΔR_{NL} .

Quenching local moments and restoring $\Delta R_{NL}(T)$. Having identified the Kondo effect at FM/NM interfaces as the key factor in the low T downturn in ΔR_{NL} , it is natural to consider whether this effect, which is deleterious in terms of maximizing spin signals, can be mitigated. Although it is clear that pure Al channels provide one means to do so, a more general approach, compatible with any channel material, would be preferable. To this end, we pursued insertion of thin Al ILs between FM and NM, the low solubility of transition metal FMs in Al minimizing interdiffusion, whereas the properties of Al eliminate local moment formation and Kondo effects. Fe/Cu NLSVs were thus fabricated with a $\sim 5\text{-nm}$ thick IL between the Fe and Cu (see Methods, and the schematic in Fig. 4b). Simple calculations establish that contributions to the spin transport from the IL in comparison to the bulk of the Cu channel can safely be neglected (Supplementary Fig. 8 and Supplementary Note 8). Figure 4b compares ΔR_{NL} at $d = 250\text{nm}$ for Fe/Cu and Fe/Al IL/Cu devices. The data are scaled to overlap at high T ($> 150\text{K}$), in order to easily assess the impact of the Al IL on the low T ΔR_{NL} . Remarkably, the low T Kondo suppression of the spin accumulation is almost completely removed by an IL of only 5nm . Defining δR_{NL} as the difference between the high- T -scaled $\Delta R_{NL}(T)$ for Fe/Al IL/Cu and Fe/Cu devices (Fig. 4b), we plot in Fig. 4c $\delta R_{NL}(T)$, normalized to its 5K value, for several d . Not only do the data collapse to a single universal curve, but also, as demonstrated by the fit, the behaviour around T_K is well described by logarithmic scaling. Specifically, the solid line is a fit to $\delta R_{NL} = a[1 - b \log(T/T_K)]$ with $T_K = 30\text{K}$, the accepted value for

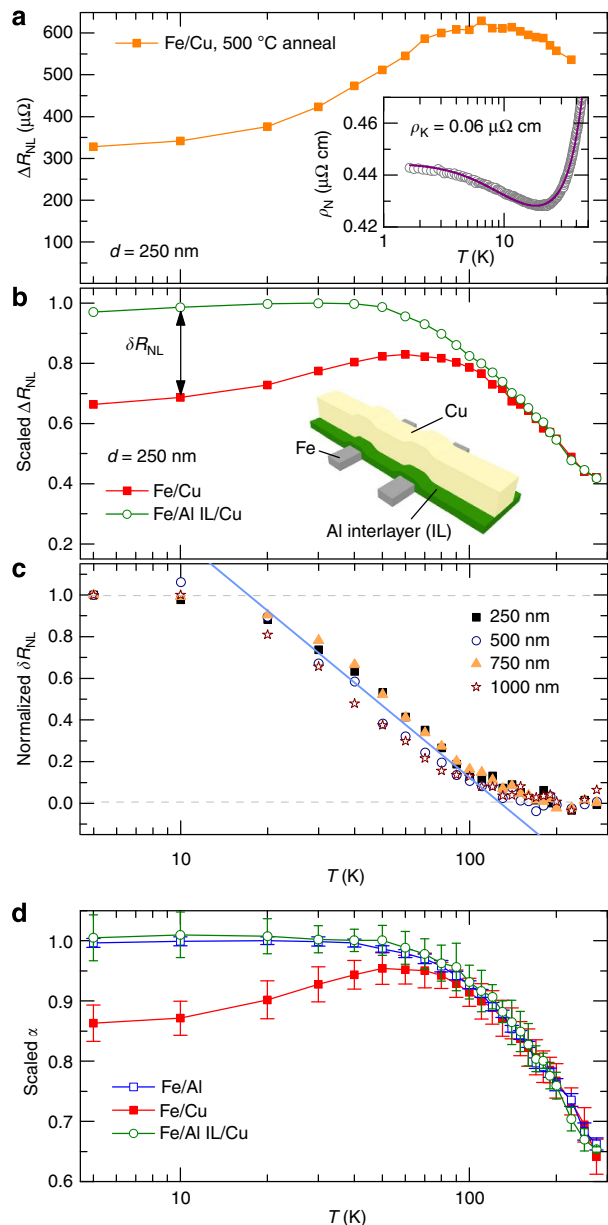


Figure 4 | Effect of annealing and Al interlayer insertion on spin transport. (a) Spin accumulation signal, ΔR_{NL} , as a function of temperature, T , for an Fe/Cu device with ferromagnet separation, $d = 250$ nm, annealed at 500°C under high vacuum for 2 h. Inset: an example of non-magnetic metal (NM) resistivity, $\rho_{\text{N}}(T)$, for such a device (grey circles), demonstrating a Kondo upturn. Data are fit using an empirical Kondo model (purple solid line). (b) T dependence of ΔR_{NL} for $d = 250$ nm Fe/Cu devices (solid red squares) and devices with an ~ 5 -nm thick Al interlayer (Fe/Al IL/Cu, green open circles). Values are scaled to Fe/Al IL/Cu at high- T ($T > 150$ K) for comparison. Inset: schematic of the non-local spin valve geometry with a thin (~ 5 nm) Al interlayer between the FM and NM. (c) Difference in ΔR_{NL} between Fe/Cu and Fe/Al IL/Cu devices, δR_{NL} as a function of T , for various FM separations, d . Solid line is a fit of all data to $\delta R_{\text{NL}} = a[1 - b \log(T/T_K)]$, where T_K is the Kondo temperature for Fe/Cu and a , b are free parameters. (d) Comparison of current polarization, $\alpha(T)$, obtained from fitting the NLSV separation dependence for Fe/Al (open blue squares), Fe/Cu (solid red squares) and Fe/Al IL/Cu (open green circles). All values are scaled to the Fe/Al high- T data for comparison. Error bars on the fit parameters are the standard errors from a least squares fit of the experimental data (appropriately weighted by combining in quadrature the standard error in the spin accumulation signal with systematic uncertainties in the device geometry).

Fe in Cu. Such a logarithmic form around T_K , with expected negative and positive deviations below and above T_K , respectively, is a commonly used phenomenological description of Kondo physics^{44,50}, and can be rationalized from equation (1) assuming $\delta\alpha \propto [1 - A \log(T/T_K)]$, that is, a Kondo-related suppression of α . An understanding beyond simple phenomenology will require an approach sophisticated enough to capture the T -dependent influence of local moments and their associated conduction electron screening, as was achieved in the normal Kondo effect via higher-order perturbation theory. That the effect we see here is certainly dominated by α , however, is emphasized in Fig. 4d, where $\alpha(T)$, scaled to its maximum value, is plotted for Fe/Al, Fe/Cu and Fe/Al IL/Cu. These data result from a large set of $\Delta R_{\text{NL}}(T, d)$ data (Supplementary Fig. 8 and Supplementary Note 8). The 5-nm thick IL in the Fe/Al IL/Cu device almost completely restores $\alpha(T)$ to the monotonic form found in Fe/Al. We note that tunnel barriers between the FM and NM^{5,13,14,25,36,50} could have a similar role, provided they prevent even minor NM/FM contamination.

Discussion

In summary, we have proposed a solution to the long-standing puzzle of the non-monotonicity of the T -dependence of the spin accumulation signal in metallic NLSV devices, the essential concept being a novel manifestation of the Kondo effect. In essence, we propose that in FM/NM combinations where the FM forms local moments when diluted in the NM, Kondo screening of the spin-disordered local moments leads to suppression of the injection/detection efficiency, and to some extent the NM spin diffusion length, around the Kondo temperature. We have further demonstrated a simple means to mitigate this effect, via insertion of a thin non-moment-supporting layer between the FM and NM. In addition to providing a solution to this immediate problem, and posing a significant challenge for future theoretical work, we propose that this work also highlights a number of potential new directions at the interface between spintronics and Kondo physics^{54,55}. We imagine future research to more fully explore the impact of Kondo physics on spin transport in metallic hetero- and nano-structures, as well as the reciprocal effects of spin injection and relaxation on Kondo systems. Significantly, the potential relevance of these ideas to room temperature spin transport should also be explored. Common systems such as Ni/Cu, Co/Cu and Co/Au possess very high Kondo temperatures, raising the possibility that physics of the type elucidated here could be suppressing spin accumulation even at room temperature.

Methods

Device fabrication. NLSV devices were fabricated on Si/Si-N(2,000 Å) substrates using a Vistec EBPG5000+ electron beam lithography tool with a PMGI/PMMA bilayer resist stack. Clean, transparent FM/NM interfaces were achieved by multi-angle deposition^{7,37}, without breaking vacuum, with the FM deposited at an angle of 49° and the NM at normal incidence. That the transparent interface limit²⁰⁻²² was achieved was explicitly verified by FM/NM contact resistance, Hanle effect and $\Delta R_{\text{NL}}(d)$ measurements (see Supplementary Figs 1 and 2). All materials were deposited in the same vacuum system (base pressure $O(10^{-10})$ Torr), using electron beam (for Al, Co, Cu, Fe, Ni, $\text{Ni}_{80}\text{Fe}_{20}$) or thermal (for Cu) evaporation. Deposition rates for NM and FM materials were 1.0 and 0.5 \AA s^{-1} , respectively, with growth pressures from 8×10^{-10} to 1×10^{-8} Torr. Nominal purities for the FM and NM materials were 99.95% and 99.999%, respectively. Film thicknesses were calibrated using *ex situ* grazing incidence X-ray reflectivity and monitored during deposition using a quartz crystal monitor. Patterned wire widths and separations were directly measured via scanning electron microscopy ($w_{\text{N}} = 150\text{--}200$ nm, $w_{\text{FM,inj}} = 150$ nm and $w_{\text{FM,det}} = 100$ nm). A domain wall nucleation pad was incorporated into FM_{inj} to reduce its coercivity and enable the AP state to be reliably obtained.

Transport measurements and fitting. Transport measurements were performed with 13 Hz AC excitation, at bias currents from $100 \mu\text{A}$ to 1 mA. At low T , careful checks for self-heating were carried out. Measured ΔR_{NL} values were corrected for

small (<10%) sample-to-sample variations in ρ and w_N using the scaling expected from equation 1. For Hanle measurements, data were acquired in both the P and AP states (as shown in Fig. 1d). The difference between these two signals (Fig. 3c,d) removes any background associated with FM rotation and leaves only the spin precession component³⁷. Note that the data presented in Fig. 3c,d are averages from positive and negative H_{\perp} sweeps. These data were fit to a solution of the spin-precession-diffusion equation, taking into account finite contact size and rotation of the magnetization of the FM electrodes:

$$\Delta R_{\text{NL}}(H_{\perp}) = S_0 \int_{-w_{\text{FM}}^{\text{inj}}}^0 \int_d^{d+w_{\text{FM}}^{\text{det}}} \int_0^{\infty} \frac{1}{\sqrt{4\pi Dt}} \exp\left[-\frac{(x_{\text{inj}} - x_{\text{det}})^2}{4Dt}\right] \cos(\omega_L t) \exp\left(-\frac{t}{\tau_s}\right) dt dx_{\text{det}} dx_{\text{inj}}, \quad (2)$$

where ω_L is the Larmor frequency ($\omega_L = \gamma B$, with γ the gyromagnetic ratio and B the magnetic flux density), t is the spin transit time, S_0 is a scaling term to account for the zero-field spin signal and x_{det} (x_{inj}) accounts for integration of the signal over the finite detector (injector) contact width. Note that this model does not take into account the effect of back-diffusion of spins into the FMs (that is, spin sinking). However, by d -dependent Hanle measurements, we have verified that the large separations reported here ($d = 2 \mu\text{m}$) are in the NM-channel-dominated regime, where spin sinking is negligible²³. For fitting, $D(T)$ is determined from the experimental $\rho_N(T)$ using a form of the Einstein relation, $\rho_N(T)^{-1} = e^2 N(E_F) D(T)$, where $N(E_F)$ is the density-of-states at the Fermi level. Note that the displayed curves (Fig. 3c,d) use a slightly suppressed M_s to phenomenologically account for in-plane rotation and demagnetization of the FM electrodes. The fitting results are quite insensitive to this value of M_s , however, and, although the fit quality suffers, using standard literature values for M_s does give quantitatively similar results for τ_s .

The Fe/Cu devices for which data are shown in Fig. 4a were annealed in high vacuum (base pressure 10^{-7} Torr). The low T resistivity was fit using a phenomenological model for the Kondo contribution to the resistivity⁵¹:

$$\rho(T) = \rho_0 + AT^2 + BT^5 + \rho_K \left[\frac{T_K^2}{T^2 + T_K^2} \right]^s, \quad (3)$$

with $T_K^s = T_K / \sqrt{2^{1/s} - 1}$. ρ_0 describes the impurity scattering contribution to ρ , whereas A and B account for electron-electron and electron-phonon scattering. We fix $s = 0.225$ and $T_K = 30$ K from literature values to obtain the Kondo resistivity ρ_K .

IL device fabrication. For the devices with an IL, a ~ 5 -nm thick Al layer was grown after FM deposition. To ensure appropriate coverage of the FM/NM interface region (that is, a layer width $> w_N$, see inset to Fig. 4a), this was done in discrete steps between -3° and $+3^\circ$ from normal incidence. Al was chosen as the IL material for several reasons: Fe atoms that diffuse into Al will not form local moments; the diffusivity of Fe in Al is substantially lower than it is in Cu and the use of a thin ($t \ll \lambda_N$), low ρ_N material such as Al should not otherwise alter the magnitude or T -dependence of the spin accumulation.

References

1. Gijs, M. A. M. & Bauer, G. E. W. Perpendicular giant magnetoresistance of magnetic multilayers. *Adv. Phys.* **46**, 285–445 (1997).
2. Yamada, M. *et al.* Scalability of spin accumulation sensor. *IEEE Trans. Magn.* **49**, 713–717 (2013).
3. Elliott, R. J. Theory of the effect of spin-orbit coupling on magnetic resonance in some semiconductors. *Phys. Rev.* **96**, 266–279 (1954).
4. Jedema, F., Nijboer, M., Filip, A. & van Wees, B. Spin injection and spin accumulation in all-metal mesoscopic spin valves. *Phys. Rev. B* **67**, 085319 (2003).
5. Idzuchi, H., Fukuma, Y., Wang, L. & Otani, Y. Spin relaxation mechanism in silver nanowires covered with MgO protection layer. *Appl. Phys. Lett.* **101**, 022415 (2012).
6. Idzuchi, H., Fukuma, Y., Wang, L. & Otani, Y. Spin injection into magnesium nanowire. *IEEE Trans. Magn.* **47**, 1545–1548 (2011).
7. Ji, Y., Hoffmann, A., Jiang, J. S., Pearson, J. E. & Bader, S. D. Non-local spin injection in lateral spin valves. *J. Phys. D: Appl. Phys.* **40**, 1280–1284 (2007).
8. Villamor, E., Isasa, M., Hueso, L. E. & Casanova, F. Contribution of defects to the spin relaxation in copper nanowires. *Phys. Rev. B* **87**, 094417 (2013).
9. Mihajlović, G., Pearson, J. E., Bader, S. D. & Hoffmann, A. Surface spin flip probability of mesoscopic Ag wires. *Phys. Rev. Lett.* **104**, 237202 (2010).
10. Kimura, T., Sato, T. & Otani, Y. Temperature evolution of spin relaxation in a NiFe/Cu lateral spin valve. *Phys. Rev. Lett.* **100**, 066602 (2008).
11. Godfrey, R. & Johnson, M. Spin Injection in mesoscopic silver wires: experimental test of resistance mismatch. *Phys. Rev. Lett.* **96**, 136601 (2006).
12. Garzon, S., Žutić, I. & Webb, R. Temperature-dependent asymmetry of the nonlocal spin-injection resistance: evidence for spin nonconserving interface scattering. *Phys. Rev. Lett.* **94**, 176601 (2005).
13. Valenzuela, S. O. & Tinkham, M. Spin-polarized tunneling in room-temperature mesoscopic spin valves. *Appl. Phys. Lett.* **85**, 5914–5916 (2004).

14. Poli, N., Urech, M., Korenivski, V. & Haviland, D. B. Spin-flip scattering at Al surfaces. *J. Appl. Phys.* **99**, 08H701 (2006).
15. Erekhinsky, M., Sharoni, A., Casanova, F. & Schuller, I. K. Surface enhanced spin-flip scattering in lateral spin valves. *Appl. Phys. Lett.* **96**, 022513 (2010).
16. Niimi, Y. *et al.* Experimental verification of comparability between spin-orbit and spin-diffusion lengths. *Phys. Rev. Lett.* **110**, 016805 (2013).
17. Monod, P. & Beuneu, F. Conduction-electron spin flip by phonons in metals: analysis of experimental data. *Phys. Rev. B* **19**, 911–916 (1979).
18. Zou, H. & Ji, Y. The origin of high surface spin-flip rate in metallic nonlocal spin valves. *Appl. Phys. Lett.* **101**, 082401 (2012).
19. Van Son, P., van Kempen, H. & Wyder, P. Boundary resistance of the ferromagnetic-nonferromagnetic metal interface. *Phys. Rev. Lett.* **58**, 2271–2273 (1987).
20. Valet, T. & Fert, A. Theory of the perpendicular magnetoresistance in magnetic multilayers. *Phys. Rev. B* **48**, 7099–7113 (1993).
21. Takahashi, S. & Maekawa, S. Spin injection and detection in magnetic nanostructures. *Phys. Rev. B* **67**, 052409 (2003).
22. Kimura, T., Hamrle, J. & Otani, Y. Estimation of spin-diffusion length from the magnitude of spin-current absorption: Multiterminal ferromagnetic/nonferromagnetic hybrid structures. *Phys. Rev. B* **72**, 014461 (2005).
23. Maassen, T., Vera-Marun, I. J., Guimarães, M. H. D. & van Wees, B. J. Contact-induced spin relaxation in Hanle spin precession measurements. *Phys. Rev. B* **86**, 235408 (2012).
24. Johnson, M. & Silsbee, R. H. Interfacial charge-spin coupling: Injection and detection of spin magnetization in metals. *Phys. Rev. Lett.* **55**, 1790–1793 (1985).
25. Jedema, F. J., Filip, A. T. & van Wees, B. J. Electrical spin injection and accumulation at room temperature in an all-metal mesoscopic spin valve. *Nature* **410**, 345–348 (2001).
26. Bakker, F., Slachter, A., Adam, J.-P. & van Wees, B. Interplay of Peltier and seebeck effects in nanoscale nonlocal spin valves. *Phys. Rev. Lett.* **105**, 136601 (2010).
27. Slachter, A., Bakker, F. L., Adam, J.-P. & van Wees, B. J. Thermally driven spin injection from a ferromagnet into a non-magnetic metal. *Nat. Phys.* **6**, 879–882 (2010).
28. Yang, T., Kimura, T. & Otani, Y. Giant spin-accumulation signal and pure spin-current-induced reversible magnetization switching. *Nat. Phys.* **4**, 851–854 (2008).
29. Mihajlović, G. *et al.* Enhanced spin signals due to native oxide formation in Ni₈₀Fe₂₀/Ag lateral spin valves. *Appl. Phys. Lett.* **97**, 112502 (2010).
30. Otani, Y. & Kimura, T. Manipulation of spin currents in metallic systems. *Philos. Trans. A Math. Phys. Eng. Sci.* **369**, 3136–3149 (2011).
31. Erekhinsky, M., Casanova, F., Schuller, I. K. & Sharoni, A. Spin-dependent Seebeck effect in non-local spin valve devices. *Appl. Phys. Lett.* **100**, 212401 (2012).
32. Casanova, F., Sharoni, A., Erekhinsky, M. & Schuller, I. Control of spin injection by direct current in lateral spin valves. *Phys. Rev. B* **79**, 184415 (2009).
33. Kimura, T., Hashimoto, N., Yamada, S., Miyao, M. & Hamaya, K. Room-temperature generation of giant pure spin currents using epitaxial Co₂FeSi spin injectors. *NPG Asia Mater.* **4**, e9 (2012).
34. Ji, Y., Hoffmann, A., Jiang, J. S. & Bader, S. D. Spin injection, diffusion, and detection in lateral spin-valves. *Appl. Phys. Lett.* **85**, 6218–6220 (2004).
35. Kimura, T. & Otani, Y. Large spin accumulation in a permalloy-silver lateral spin valve. *Phys. Rev. Lett.* **99**, 196604 (2007).
36. Fukuma, Y. *et al.* Giant enhancement of spin accumulation and long-distance spin precession in metallic lateral spin valves. *Nat. Mater.* **10**, 527–531 (2011).
37. Jedema, F. J., Costache, M. V., Heersche, H. B., Baselmans, J. J. A. & van Wees, B. J. Electrical detection of spin accumulation and spin precession at room temperature in metallic spin valves. *Appl. Phys. Lett.* **81**, 5162–5164 (2002).
38. Beuneu, F. & Monod, P. The Elliott relation in pure metals. *Phys. Rev. B* **18**, 2422–2425 (1978).
39. Mihajlović, G. *et al.* Magnetic-field enhancement of nonlocal spin signal in Ni₈₀Fe₂₀/Ag lateral spin valves. *Phys. Rev. B* **84**, 132407 (2011).
40. Shang, C., Nowak, J., Jansen, R. & Moodera, J. Temperature dependence of magnetoresistance and surface magnetization in ferromagnetic tunnel junctions. *Phys. Rev. B* **58**, R2917–R2920 (1998).
41. Bänninger, U., Busch, G., Campagna, M. & Siegmann, H. Photoelectron spin polarization and ferromagnetism of crystalline and amorphous nickel. *Phys. Rev. Lett.* **25**, 585–587 (1970).
42. Meservey, R. & Tedrow, P. M. Spin-polarized electron tunneling. *Phys. Rep.* **238**, 173–243 (1994).
43. Bass, J. & Pratt, W. P. Spin-diffusion lengths in metals and alloys, and spin-flipping at metal/metal interfaces: an experimentalist's critical review. *J. Phys. Condens. Matter* **19**, 183201 (2007).
44. Mydosh, J. A. *Spin Glasses: An Experimental Introduction* (Taylor & Francis, 1993).
45. Gruner, G. & Zawadowski, A. Magnetic impurities in non-magnetic metals. *Reports Prog. Phys.* **37**, 1497–1583 (1974).

46. Kondo, J. *The Physics of Dilute Magnetic Alloys* (Cambridge University Press, 2012).
47. Wei, W. & Bergmann, G. CuCo: a new surface Kondo system. *Phys. Rev. B* **37**, 5990–5993 (1988).
48. Taniyama, T., Fujiwara, N., Kitamoto, Y. & Yamazaki, Y. Asymmetric transport due to spin injection into a Kondo alloy. *Phys. Rev. Lett.* **90**, 016601 (2003).
49. Inoue, K. & Nakamura, Y. Kondo-type resistivity anomaly in noble metal alloys with 3d metals. *Phys. Status Solidi* **58**, 355–369 (1973).
50. Lee, K. *et al.* Kondo effect in magnetic tunnel junctions. *Phys. Rev. Lett.* **98**, 107202 (2007).
51. Goldhaber-Gordon, D. *et al.* From the Kondo regime to the mixed-valence regime in a single-electron transistor. *Phys. Rev. Lett.* **81**, 5225–5228 (1998).
52. Franck, J. P., Manchester, F. D. & Martin, D. L. The specific heat of pure copper and of some dilute copper + iron alloys showing a minimum in the electrical resistance at low temperatures. *Proc. R. Soc. A Math. Phys. Eng. Sci.* **263**, 494–507 (1961).
53. Villamor, E., Isasa, M., Hueso, L. E. & Casanova, F. Temperature dependence of spin polarization in ferromagnetic metals using lateral spin valves. *Phys. Rev. B* **88**, 184411 (2013).
54. Pasupathy, A. N. *et al.* The Kondo effect in the presence of ferromagnetism. *Science* **306**, 86–89 (2004).
55. Yang, H., Yang, S.-H. & Parkin, S. S. P. Crossover from Kondo-assisted suppression to co-tunneling enhancement of tunneling magnetoresistance via ferromagnetic nanodots in MgO tunnel barriers. *Nano Lett.* **8**, 340–344 (2008).

Acknowledgements

This project was funded by the NSF MRSEC under award DMR-0819885 and a Marie Curie International Outgoing Fellowship within the 7th European Community

Framework Programme (project no. 299376). Research at the ORNL Spallation Neutron Source ORNL was sponsored by the Scientific User Facilities Division, Office of Basic Energy Sciences, US Department of Energy. ORNL is managed by UT-Battelle, LLC, under contract DE-AC05-00OR22725 with the US Department of Energy. Parts of this work were carried out in the Characterization Facility, University of Minnesota, which receives partial support from NSF through the MRSEC program. Parts of this work were carried out in the Minnesota Nano Center, which receives partial support from the NSF through the NNIN program.

Author contributions

NLSV fabrication, measurement and analysis were performed by L.O'B., D.S. and M.J.E., under the supervision of C.L. and P.A.C. PNR measurements and analysis were performed by L.O'B., R.J.G. and H.A., under the supervision of C.L. and V.L. C.L. and P.A.C. initiated the study. L.O'B. and C.L. wrote the manuscript, with contributions from all authors.

Additional information

Supplementary Information accompanies this paper at <http://www.nature.com/naturecommunications>

Competing financial interests: The authors declare no competing financial interests.

Reprints and permission information is available online at <http://npj.nature.com/reprintsandpermissions/>

How to cite this article: O'Brien, L. *et al.* Kondo physics in non-local metallic spin transport devices. *Nat. Commun.* 5:3927 doi: 10.1038/ncomms4927 (2014).